Coupled mechanical and chemical processes in engineered geothermal reservoirs with dynamic permeability

Joshua Taron [a,b,*], Derek Elsworth [a]

[a] Department of Energy and Mineral Engineering and Center for Geomechanics, Geofluids, and Geohazards (G3), Pennsylvania State University, University Park, PA, USA
[b] Department of Environmental Informatics, Helmholtz Center for Environmental Research (UFZ), Leipzig, Germany

ABSTRACT

A model is developed to represent mechanical strain, stress-enhanced dissolution, and shear dilation as innately hysteretic and interlinked processes in rough contacting fractures. The model is incorporated into a numerical simulator designed to examine permeability change and thermal exchange in chemically active and deformable fractured reservoirs. A candidate engineered geothermal reservoir system (EGS) is targeted. The mechanistic model is able to distinguish differences between the evolution of fluid transmission characteristics of (1) small scale, closely spaced fractures, and (2) large-scale, more widely spaced fractures. Alternate realizations of fracture frequency and scale, exhibiting identical initial bulk permeability, lead to significantly different conclusions regarding permeability evolution and thermal drawdown within the reservoir. Reactivation, primarily through mechanical shear, of pervasive, large-scale fractures is shown capable of causing both hydraulic and thermal short circuiting. Small variations in fracture scale impact the balance between the efficiency of thermal transfer and the rate of fluid circulation. Stress-enhanced chemical dissolution, initially at equilibrium within the reservoir, may be reactivated as fractures are forced out of equilibrium during hydraulic fracturing. At the conditions examined (250 °C reservoir with 70 °C injection), however, shear dilation exerts dominant control over changes to permeability. Heterogeneity in permeability, generated from a normal distribution of fracture spacing, impacts thermal breakthrough times at the withdrawal well, as well as withdrawal rates. For the given conditions, spatial variability over ∼1 order of magnitude leads to a reduction of ∼10% in withdrawal rates compared to a spatially uniform system. Permeability is a strongly dynamic property and at geothermal conditions is influenced by the full suite of THMC interactions.

1. Introduction

The critical role of fractures in controlling the mechanical and hydraulic properties of discontinuous rock masses is well known [1,2]. When subjected to external (engineered) stresses much of the physical and chemical response is concentrated within these fractures that are, in general, more hydraulically conductive and mechanically compliant than the surrounding rock.

In applications such as enhanced geothermal systems (EGS) and reservoirs for the sequestration of CO_2 fluid transmission characteristics define the utility of the reservoirs for such purposes: understanding the response of fractures, faults, and bedding planes to external stresses is vital to engineering design. EGS in particular exhibits processes activated by thermal, hydraulic, mechanical, and chemical forces, so that fracture behavior is non-linear and difficult to predict. Only recently have numerical models been extended to allow contribution from all four conservation systems (THMC), and become capable of examining in unison the most active processes in permeability change; thereby distinguishing those with greatest influence.

This work presents a method to combine elastic deformation, chemical–mechanical creep (CM creep), mineral reaction, and shear in rough fractures. Fractures deform mechanically via contact theory and Boussinesq half-space deformation. The contact-area-based mechanism allows for direct extension to stress dissolution (CM creep) and shear dilation, based on direct measurement of fracture surfaces (profiles), while reservoir scale extension occurs via the THMC simulator of [3]. Simulations utilize a spatial distribution of fracture properties and anisotropically evolving permeability: aperture changes occur at different rates on orthogonal fractures. The contact area model allows the examination not only of bulk permeability change, but also the contributing mechanisms—a given magnitude of permeability due to widely spaced, highly conductive fractures exhibits

strongly different behaviors than the same bulk permeability magnitude, derived from tightly spaced, lower conductivity fractures [4,5]. In this way, one conceptualization for the development of a short-circuiting fracture network is examined.

2. Fractured rock at disequilibrium

Because fractures have a dominant influence on bulk rock properties, a large volume of previous research has focused on their hydromechanical properties, such as compressive strength [1,6,7], the effect of normal displacements and fracture roughness on permeability [7–9], shear displacement on permeability [10,11], and direct relationships between mechanical and hydraulic apertures [12–14]. Mineral precipitation and dissolution has received attention from a different angle, with two notable works relating to localized dissolution behaviors [15] and heterogeneity of mineral assemblages (thus relating to the accuracy of mineral abundance derived reactive transport simulators) [16].

Chemo-mechanical creep (CM creep) processes such as pressure solution [17] have been studied for a number of years in poromechanics. Pressure solution (PS) is known to contribute strongly as a compaction mechanism in diagenesis and fault healing [18], and often behaves similarly to creep from stress corrosion cracking [19]. In granular quartz, porosity reduction from PS can be as high as 60–70% [20] ($\sim$100 MPa, 500 °C). In fractures, although relatively fewer attempts have been made to observe CM creep behavior [21,22], more significant deformation and more rapid action has been observed. The study of [22] showed that even at modest temperatures (100–150 °C) and stresses ($\sim$3.5 MPa), a hydrated fracture can, in a single month, drop permeability by a factor of 20 at invariant stress. PS is expected to dominate CM creep behavior at temperatures nearing 300 °C in aggregated quartz [23], with stress corrosion the most likely contributor at lower values [24]. In fractures, this dividing line remains untested.

In enhanced geothermal systems (EGS) large thermal stresses arising from the injection of cold ($\sim$70 °C) water into a hot ($\sim$250 °C) reservoir introduce significant likelihood of shear failure, as indexed by observed injection-induced seismicity [25]. This thermal (and hydraulic) injection rearranges the equilibrium stress field and also introduces strong disequilibrium in chemical activity. The fracture (and thus reservoir) response to such intense forcing is extremely complex and difficult to analyze. Combining mechanical shear with normal compression has been accomplished in the mechanical sense [10], but combining an exponential fracture closure model with (irreversible) chemical–mechanical aperture change is, at least currently, generally unreasonable as they lack the ability to represent innate hysteresis. This is due to a lack of time dependency and reliance upon a stiffness coefficient that is dependent on the degree of elastic fracture closure (cumulatively, specific stiffness). Such a coefficient, however, is not constant through an irreversible change, such as plastic failure or chemical compaction. Hysteretic coupling such as this must originate in micromechanics.

3. Contributing mechanisms

Fracture closure under stress is most often addressed with (1) a laboratory derived stress-closure model, or (2) a contact model based on estimates of real contact area between rough surfaces; used to inform elastic compliance. Both methods are empirical; the former relying on laboratory information of stress and closure, and the latter relying on laboratory information of contact area and closure (fracture profiles). The fundamental difference between these two methods lies in their choice of the variable defining closure: stress in the first and contact area in the second. In the following, we utilize existing fracture profiles to inform an empirical function for contact theory (profiles could also be generated synthetically from a random surface distribution). Contact theory is chosen because of certain advantages associated with the use of contact area, rather than stress. This contact area basis allows (1) direct coupling to other contact-area-driven processes that may be mechanical and/or chemical in nature, and (2) time dependence, so that irreversible changes can be accommodated and observed as innately hysteretic deformation.

3.1. Elastic closure and contact area

As fractures dilate or compact (by any mechanism) contact area between opposing fracture surfaces is altered, leading to changes in fracture apparent stiffness. This is accommodated directly in contact models, and indirectly in stress-closure models. Stress-closure mechanical models have been addressed by several authors [1,7], often logarithmically [1]

$$db = A + B\ln\sigma', \tag{1}$$

for aperture change, db, effective normal stress, σ', and the constants A and B. Similar forms have been used to model mechanical aperture closure in fractured reservoirs [26] and extended to include thermo-chemical behaviors [27].

For aperture closure based on contact theory, deformation of each asperity is usually assumed to follow either Hertz's solution for the elastic contact of spherical bodies [28], or a model for the deformation of cylindrical columns [29–31]. Asperity deformation alone has been shown to underestimate closure at low effective stress, and overestimate at higher stress [32], with more accurate solutions obtained by considering also deformation of the (approximate) half-space surrounding each asperity [30,33]. Additional information regarding fracture closure models can be found in these cited works, and also in the review of [34].

Fracture closure is approximated here with a cylindrical model for asperity deformation and Boussinesq solution for half-space deformation surrounding each asperity. Interaction between half-space deformation at each contact [30] is not considered. Small changes to the style of deformation, such as adapting to a Hertzian model, have only minimal effects on overall behavior at the conditions examined here.

In addition to Eq. (1), another important result of Goodman's [1] experiments is that "mated" (zero shear offset) and "unmated" (finite shear offset) fractures exhibit the same closure behavior (can be represented by Eq. (1)) and merely differ proportionally with the constants, A and B (see also [35]). This suggests that the contact area relationship for any fracture (plot of real contact area versus mechanical closure) after any amount of shear will be a simple extension of the mated solution. Fig. 1 shows the contact area relationship (calculated from 3D profiles) for a natural fracture in novaculite (NV1). These were obtained by numerically mating two rough fracture surface profiles and calculating the growth of the interpenetrated area of overlap with the incremental decrease in mean separation between fracture surfaces. The fracture surface profiles were then separated to zero overlap, numerically sheared at small increments, and closed again to calculate a new area relationship at each degree of offset. The closure curve at each degree of offset (as a function of shear distance, x) can be fit with the exponential function

$$b_v = a_1(x) + a_2(x)\exp(-R_c/a_3(x)), \tag{2}$$

for the void aperture b_v, contact area ratio, R_c (ratio of real contact area to total square area of the fracture), and the constants, a_i.

Void aperture refers to the mean separation between surfaces excluding points in contact (the mean void separation) [12]. The use of this aperture, rather than the mean mechanical aperture (mean of all points), is important for corrections to hydraulic aperture [36]. Physically, a_1 refers to the minimum possible aperture, a_2 is the initial aperture minus a_1, and a_3 determines the curvature of the relationship (similar in form to fracture compliance). This relationship is identical in form to the mechanical closure relationship presented by Rutqvist et al. [26], with effective stress substituted for R_c. Fig. 2 shows the constants a_1, a_2, and a_3 as functions of shear distance from the initially mated fracture.

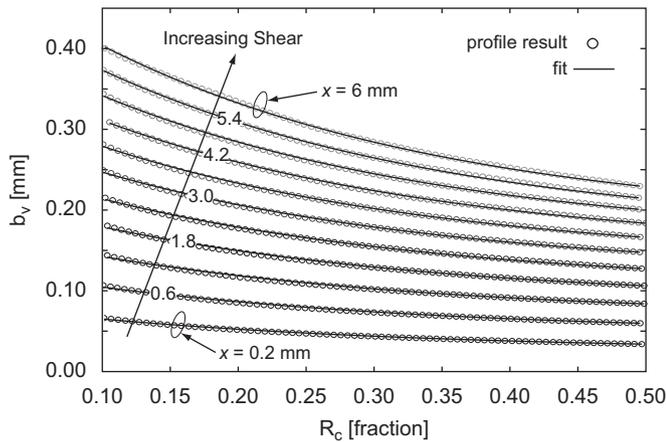This process is akin to introducing an angle of dilation for fracture shear, but the correction is non-linear and is applied at each end of the fracture closure curve. Introducing an angle of dilation, ψ, in the standard way, would imply a linear variation in a_y and a_y with x, and a_y constant. From Fig. 2 the variation in a_1 with shear is predominantly linear, while a_2 admits a quadratic profile and dilates at a much lower rate than a_1. Because a_3 is held constant in these results, the tangent to the curve $a_1(x) + a_2(x)$ represents the instantaneous angle of dilation (Fig. 2). Values of these functions are listed in Table 1 for the same fracture at three different scales of roughness (NV2 and NV3 are fractal expansions of NV1).

Contact area ratio calculated from laser profiles does not adhere exactly to an exponential/logarithmic relationship at all values of closure [37], but can be shown to follow more closely a Gaussian or chi-square distribution [34,35]. For the range of conditions examined in this work ($R_c \approx 15-45\%$), Eq. (2) is quite accurate. For lower stress ($R_c \approx 1-25\%$), behavior follows more closely the form of Eq. (1),

$$b_v = a_1 + a_2 \ln(R_c). \tag{3}$$

3.2. Stress-enhanced chemical dissolution

Pressure solution (PS) is a CM creep process that occurs when fluid saturated mineral surfaces come into contact at stresses elevated above the hydrostat. Elevated stress at these contacts increases the activity of mineral species, leading to an increased rate of chemical dissolution [38], and an increased solubility
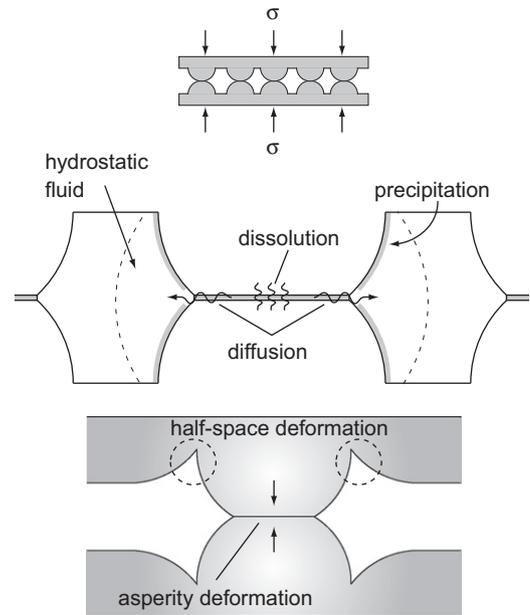

Fig. 1. Contact area curves as a function of shear distance.
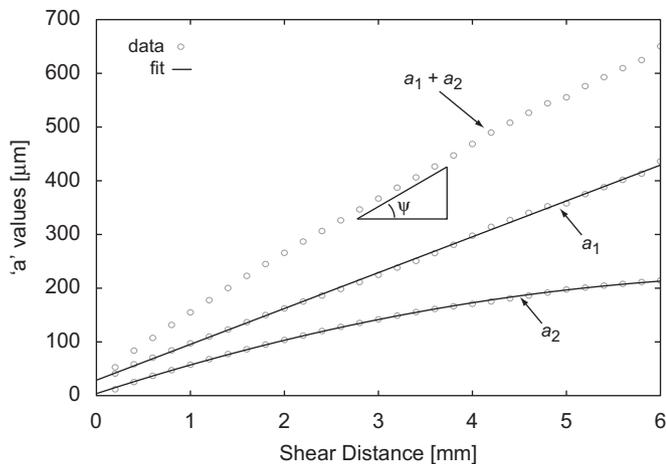
Fig. 2. Contact area coefficients calculated from the data in Fig. 1.

Fig. 3. Compaction processes: pressure solution and elastic deformation.

Table 1
Contact area relationships for several fractures. NV2 and NV3 are fractal expansions of NV1.

	s_d (mm)[a]	a_1 (µm)[b] $Ax^2 + Bx + C$			a_2 (µm)[b] $Ax^2 + B$		a_3
		A	B	C	A	B	
NV1	0.513	-3.6942×10^6	5.7074×10^4	3.6318	6.6745×10^4	28.681	0.26
NV2	1.538	-2.4314×10^6	6.3521×10^4	15.242	6.2078×10^4	102.65	0.29
NV3	2.563	-1.4528×10^6	6.3864×10^4	26.994	5.9518×10^4	184.04	0.28

[a] Standard deviation of fracture surface.
[b] For shear distance, x, in meters.

within the contacting fluids [17]. As aqueous concentrations increase, a chemical potential gradient evolves for the diffusion of species away from the contact point and, eventually, precipitation at unstressed sites in the fracture or porous media (Fig. 3). Pressure solution refers to the serial dissolution–diffusion–precipitation system.

By continuity of stress, each contact in a rough fracture experiences a stress $\sigma_a = \sigma'/R_c$, where σ' is the effective normal stress applied across the fracture. As compaction progresses, contact area increases as more asperities come into contact so that σ_a decreases. Eventually an equilibrium is obtained, where PS is no longer thermodynamically favorable, and this equilibrium stress is approximately [39,40]

$$\sigma_c = \frac{E_m(1-T/T_m)}{4V_m}, \tag{4}$$

where $E_m = 8.57 \times 10^{-3}\,\text{J}\,\text{mol}^{-1}$ is the heat of fusion, $T_m = 1883\,\text{K}$ the temperature of fusion, and $V_m = 2.27 \times 10^{-5}\,\text{m}^3\,\text{mol}^{-1}$ the molar volume (all given for cristobalite-quartz). A fully concentration dependent form for PS rate controlled by the serial processes of dissolution, diffusion, and precipitation can be found in [41,42]. However, coupling of aqueous chemical concentrations in the reactive transport simulator to those in a pressure solution model requires a greater degree of complexity than is warranted in this first analysis, and so a typical approximation for stress-enhanced dissolution is [43]

$$\dot{m}^{diss}(\text{mol/s}) = k^+ A_{rx} \frac{\Delta\mu}{RT}, \tag{5}$$

where k^+ is the dissolution rate constant, A_{rx} the reactive area, R the gas constant, T temperature, and the chemical potential difference between stressed contacts and unstressed open voids is [44,45] $\Delta\mu = V_m(\sigma_a - \sigma_c)$, for the molar volume, V_m. It can be shown [41] that Eq. (5) tends to represent a mean approximation of pressure solution, slightly underestimating rates in dissolution dominated regimes, and slightly overestimating in diffusion control. In addition, when time-scales of interest are much larger than those over which pressure solution reaches equilibrium, Eq. (5) becomes unimportant, and only Eq. (4) will control behavior. Eq. (5) is manipulated geometrically

$$\frac{db_{PS}}{dt}(\text{m/s}) = \left(k^+ A_{rx}\frac{V_m}{A_{rx}}\right)\frac{\Delta\mu}{RT} = k^+ V_m\frac{\Delta\mu}{RT}, \tag{6}$$

to represent the change of aperture due to pressure solution (subscript PS) with time. Increase in contact area with further compaction will eventually encourage equilibrium through modification of $\Delta\mu$.

3.3. Mineral precipitation/dissolution

Hydrostatic precipitation and dissolution of minerals within a cumulative fracture volume is calculated internally in TOUGH-REACT, referenced to changes in the mineral volume fraction, Δf_m. Because this does not alter asperity length (or, generally speaking, affect contact area), it need not be implicitly coupled to the above aperture change processes. Effects on fracture aperture and permeability from this process are accommodated from the deposited or removed volume of minerals. The governing equations are described in [3].

4. Coupled aperture change model

The Boussinesq solution for the deformation length (aperture change) of a half-space from a circular contact of radius, r, is [46]

$$db_B = \frac{\sigma'}{ER_c}\left[\frac{16r(1-v^2)}{3\pi}\right], \tag{7}$$

while the deformation of a cylindrical column (asperity) is

$$db_A = \frac{\sigma'}{ER_c}b_v^i, \tag{8}$$

where b_v^i is the initial void aperture (an approximation of the potential deformation length). Combining these relationships, the total elastic aperture change is

$$db_E = \frac{\sigma'}{ER_c}(D+b_v^i), \tag{9}$$

where D refers to the bracketed term in Eq. (7). Elastic aperture closure and chemo-mechanical dissolution are interdependent processes; elastic closure increases contact area, thus lowering the activation energy and increasing the rate of PS, while PS decreases the length of asperity subject to strain and increases contact area, thus lowering σ_a. In Eq. (9) b_v^i is a function of previous irreversible (from PS) aperture change. The parameter R_c depends also on previous irreversible change, and because it is not a constant during the process of mechanical deformation, mechanical closure requires a simple Newton iteration between Eqs. (9) and (2), with the full aperture change sequence illustrated in Fig. 4. For clarity, the function to be minimized is

$$f(db_E) = \frac{\sigma'}{ER_c^{k-1}}(D+b_v^i) - db_E^{k-1} = 0, \tag{10}$$

over iteration, k, and with R_c given by Eq. (2)

$$R_c^{k-1} = -a_3(x)\ln\left(\frac{b_v^i - db_E^{k-1} - a_1(x)}{a_2(x)}\right). \tag{11}$$

Permeability calculation follows the cubic law, $k = b_h^3/12s$, for fracture spacing, s, and with the hydraulic aperture correction [12]

$$b_h = b_v\left(\frac{1-R_c}{1+R_c}\right). \tag{12}$$

The character of the combined model is illustrated in Fig. 5 at a temperature of 250 °C and utilizing the contact area relationship for NV1. Dashed lines show the result of Eq. (6) only, and solid lines utilize the coupled elastic and PS model. As compaction from PS progresses, contact area is increased while the potential length of deformation, b_v^i, is decreased. Eventually pressure solution slows to equilibrium, and the final elastic deformation is small (small σ_a and small b_v^i). In other words, the process increases fracture stiffness.
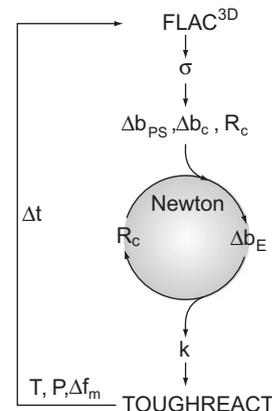

Fig. 4. Aperture change scheme. Δb_c is aperture change due to mineral precipitation/dissolution, calculated from changes to mineral volume fraction exiting from TOUGHREACT.
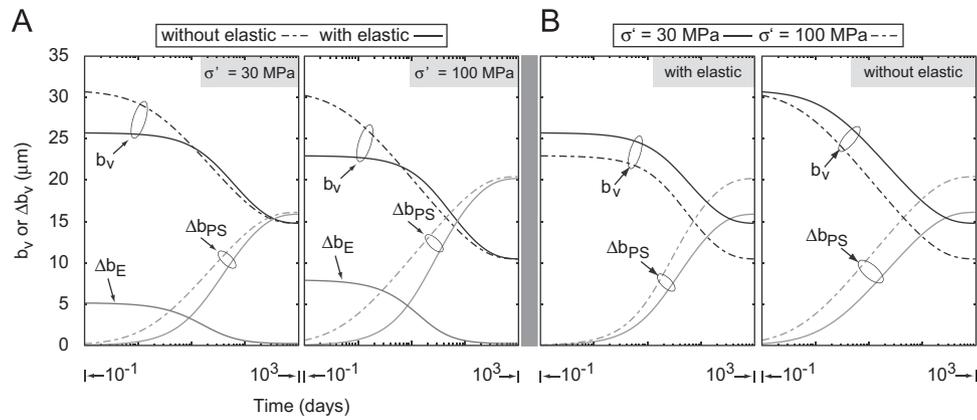
Fig. 5. Combined fracture closure from pressure solution and elastic deformation. Refer to scheme in Fig. 4. Dashed lines allow pressure solution compaction and *exclude* any mechanical equilibration. Δb_E is elastic aperture reduction. Δb_{PS} is pressure solution aperture reduction. b_v is actual void aperture. Reference: cubic law calculation gives permeability of 2.25×10^{-15} m^2 and 1.04×10^{-17} m^2 for 30 and 5 μm aperture, respectively, for fracture spacing of 1 m. Simulation data is identical in (A) and (B): cross plotted in different combinations for purpose of comparison.
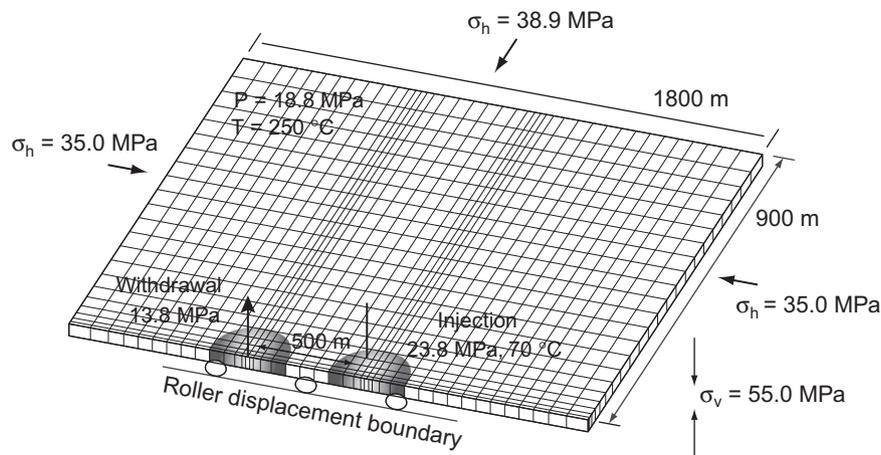

Fig. 6. Plan-view conceptualization of geothermal reservoir. Conditions and boundaries described in text.

4.1. Upscaling

Several studies have illustrated the self-affine nature of rock fracture [47,48] at small [49] and large [50] scales. In this work, fracture profiles are used directly to generate the required contact area relationships and, as an approximation of the true system, a simple fractal expansion is used to expand the profiles to a larger roughness scale and new area relationships are then generated. Fractal dimension is obtained from a log–log plot of fracture surface area versus sampling interval [49,50]. Samples NV2 and NV3 in Table 1 are expansions of NV1.

5. Simulation logic

Simulations utilize the THMC simulator presented in [3]. This modular code couples the multiphase, multi-component, non-isothermal, reactive transport, and chemical precipitation/dissolution capabilities of TOUGHREACT [51] with the stress/deformation analyses of FLAC^{3D} [52]. The flow system follows a dual-porosity, two continuum structure, while the pressure-mechanical coupling is treated as an undrained system, with dual-porosity poroelastic theory adapted from [53,54]. In a single iteration, fluid pressure builds separately in the two domains, fracture and matrix, in response to a given mechanical strain, and

this pressure is dissipated through the next iteration with the dual-porosity flow response of TOUGHREACT. Poroelastic calculations occur in a separate FORTRAN executable that also conducts linear interpolation between grid points of the two codes, modifies the explicit time step based on a history of stress tolerance, calculates pressure and temperature dependent thermodynamic compressibility of reservoir fluids, evolves fracture aperture due to mechanical and chemical processes, and applies aperture changes to the bulk permeability field.

6. Reservoir simulation

Behavior of the fracture change model and full coupled system is examined with conditions prototypical to an enhanced geothermal system (EGS) (Fig. 6). Boundary stresses are 35 MPa horizontal and 55 MPa vertical, with an initial pore pressure of 18.8 MPa and temperature of 250 °C, roughly corresponding to a depth of 2500 m in the east flank of Coso geothermal field [55]. Chemical composition is adopted for a typical granodiorite assemblage [56], and aqueous chemical compositions are obtained by equilibrating this assemblage at initial temperature and pressure with dilute water. The most active minerals under these conditions are quartz, amorphous silica, calcite, and k-feldspar [57], and these are adopted to comprise the reactive system.

Table 2
Variations in test conditions utilized in simulations.

Test	Style	Standard deviation (mm)	Fracture spacing (m)	k^{x-y} (m^2)[a,b,c]
T0	_isotropic_	1.538	1.060	8.24×10^{-15}
UT1	anisotropic	_0.513_	_1.000_	8.24×10^{-15}
UT2[d]	**anisotropic**	**1.538**	**1.445**	$\mathbf{8.24 \times 10^{-15}}$
UT3	anisotropic	_2.563_	_7.720_	8.24×10^{-15}
SS	anisotropic	1.538	1.451 ± 1.40	4.19×10^{-15} to 2.35×10^{-13}

[a] Initial x–y permeability, minimum and maximum if spatially variable.
[b] In all cases, the mean permeability (over all elements) is $8.24 \times 10^{-15} \pm 0.01 \times 10^{-15}$.
[c] Permeability refers to the post equilibration (pressure solution equilibrium obtained) permeability.
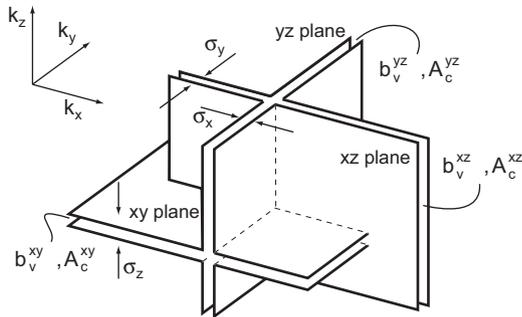[d] Moderate fracture spacing case, for comparison to T0 and SS.

Fig. 7. Conceptualization of anisotropic permeability occurring on three orthogonal fracture planes.

A single injection well 0.2 m in diameter injects water at 70 °C and acts as a constant pressure source of 23.8 MPa. A companion withdrawal well is separated by 500 m, and serves as a Dirichlet sink of 13.8 MPa. Chemical composition of the injection water is obtained by extracting the initial reservoir water (previous paragraph) and allowing equilibration at 70 °C without the presence of reactive minerals for 1 h (allowing precipitation and concentration change). The wells are located on a boundary of symmetry (zero flux, roller stress), while other xy-plane boundaries assume an infinite reservoir (maintaining initial temperature and pressure), and the top and bottom boundaries are zero flux. Several test runs were conducted to guarantee the lack of boundary interference, and the full geometric size accommodated appropriately. Plan-view contour plots examined below are zoomed in to highlight behavior, and represent only a portion of the total model domain. We refer the reader to [58] for an analysis of the sensitivity of input parameters in geothermal reservoirs.

Fracture characteristics listed in Table 1 represent composite fracture system, with reference to Table 2 listing variations in test conditions. The fracture sample is a natural calcite-infilled fracture of Arkansas novaculite, and is only assumed an analogue to the real fracture system. This is equivalent to approximating fracture stiffness, but in this case the stiffness is provided by a representative contact area function. Future tests will seek to constrain the importance of this fracture selection, and examine the use of alternatives. Fractures are allowed to achieve equilibrium closure (mechanically and chemically) prior to beginning the simulation (i.e. Fig. 5).

Following equilibration, permeability in the reservoir is far lower than necessary for reasonable withdrawal rates. The existing fracture set was hydraulically stimulated (fracture propagation is not considered) by increasing the injection pressure above _in situ_ stresses for several cycles of ∼6 min. The result is an initial profile of unmated fractures of higher permeability. For all comparative simulations, the same initial (post-hydraulic fracture) permeability is applied to injection and withdrawal to allow comparison of reservoir behavior from the same initial value. Therefore, the characteristics of the
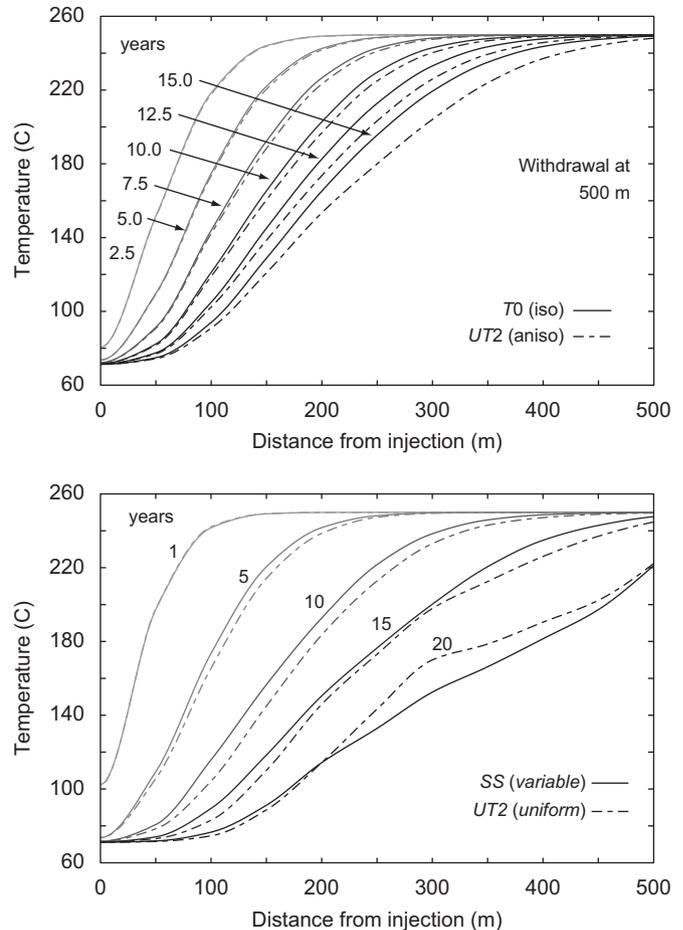

Fig. 8. Temperature evolution between injection and withdrawal for isotropy (T0, solid lines) and anisotropy (UT2, dashed) from 0 to 15 years (top), and for spatially heterogeneous (SS, solid lines) and uniform (UT2, dashed) permeability (bottom).

hydraulic fracture itself are not important to the comparative results presented below. We note that the current model is not optimally designed for rapid hydraulic fracturing, where very rapid mechanical changes extend simulation times significantly (the mechanical to hydraulic time step is controlled by the stress loading rate [3]).

6.1. Shear failure

Failure calculations are handled with FLAC^{3D} utilizing a Mohr–Coulomb failure criterion and non-associated flow rule. Fracture propagation is not considered; an existing fracture set is assumed to absorb the energy of failure through plastic flow. Friction angle is assumed constant (35°), while the angle of dilation utilized in

mechanical failure calculations is extracted from an incremental forward projection of Eq. (2), and then input to FLAC³ᴰ. In the flow system, a dilation angle is not required because fracture aperture is implicitly dilated in Eq. (2).

6.2. Anisotropy and spatial variability

Anisotropic permeability as conceptualized here is illustrated in Fig. 7. Use of this term implies that fracture compression and dilation occurs differently on three, mutually orthogonal fracture planes, as a function of the normal stress on that plane and current isotropic conditions of temperature and pressure. Therefore, contact area evolves at different rates on each plane, affecting both the rate of pressure solution and the state of elastic compression. Shear dilation is addressed via the plastic flow vector, segmented into its Cartesian components and these components applied to their corresponding fracture plane. Permeability follows the cubic law, with hydraulic aperture correction. See [59] for a discussion of cubic law averaging applied to fracture sets of variable aperture.

Comparisons of test T0 with its anisotropic companion, UT2, (Fig. 8) do not indicate the isotropic solution to be of significantly lower quality than a fully anisotropic one. As a potential caveat to this result, these simulations are conducted in pseudo-3D plan-view, so that the maximum principal stress is nearly always oriented in the vertical (out of the plane of Fig. 9). A fully 3D analysis may exhibit greater anisotropic variability. As the anisotropic extension does not contribute significantly to computational load, it is utilized exclusively in all remaining simulations.

6.3. Spatial heterogeneity

Permeability is highly variable in fractured geologies. With the large influx of cold water associated with EGS systems, pre-existing pockets of low or high permeability could have significant consequences for the evolution of shear stresses and plastic failure. High-permeability zones will allow the rapid influx of cold water via flow-conductive fractures, and subsequent stress disequilibrium with neighboring regions. Areas of low permeability will serve, in a dual-porosity system, as significant storage sites for hot reservoir fluids, thus exhibiting similar stress disequilibrium with surroundings that are infiltrated more quickly by cooler water.

The permeability model introduced previously does not allow the direct insertion of a permeability field, because the permeability depends intrinsically on fracture contact area and the factors contributing to its current state. Mechanistically, this mirrors behavior in a natural reservoir, where bulk permeability will be spatially variable, predominantly, by the contribution of three factors: fracture scale, fracture offset, and fracture spacing. Any of these may be adapted spatially in the above model. The most straightforward and easily definable of these is fracture spacing. To introduce heterogeneous permeability, fracture spacing is sampled from a normal distribution over the range outlined in Table 2. We note that this is only an approximation of true field scale variability that, in reality, will depend on all three contributing and correlated properties.

The effect of heterogeneity on the advancement of the thermal front is shown in Fig. 8, which compares the uniform permeability
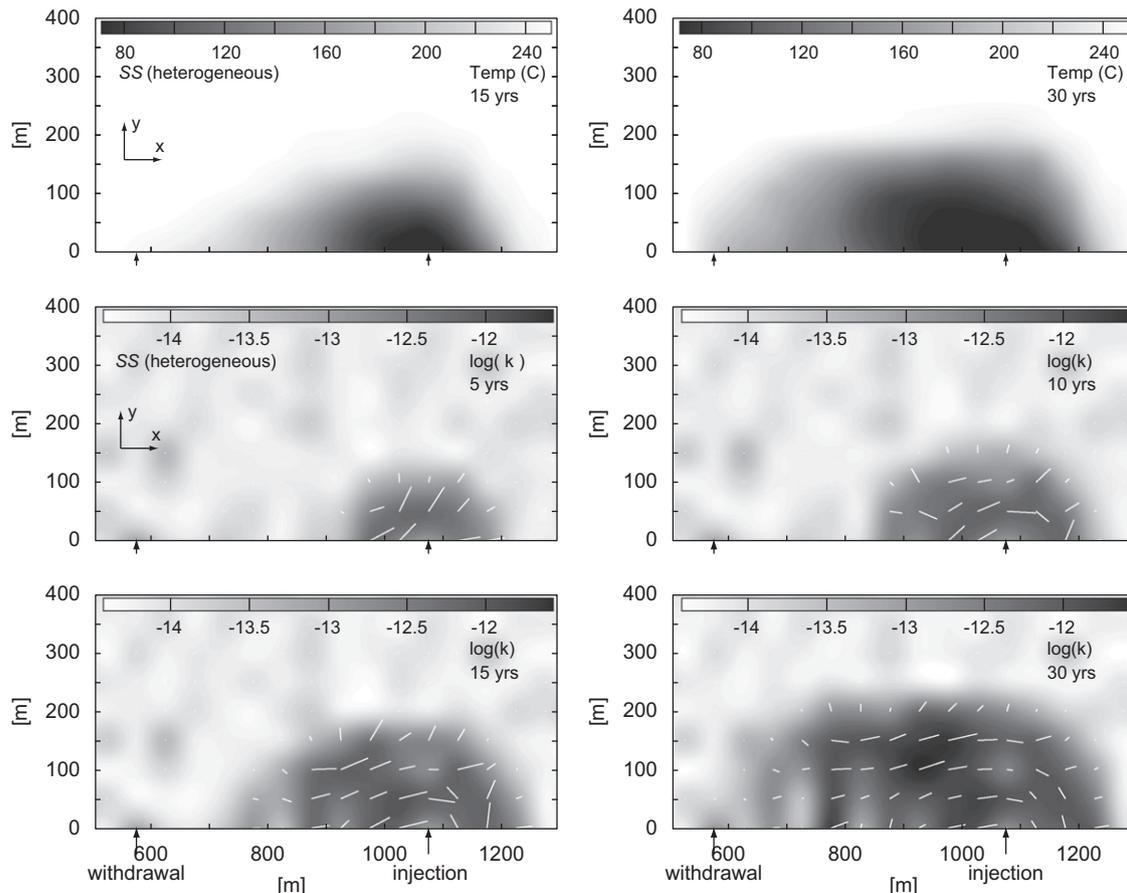

Fig. 9. Temperature (top) and permeability (bottom) evolution for 5–30 years, in all cases utilizing test SS (spatially variable, anisotropic). White vectors indicate locations undergoing shear. Orientation represents the Coulomb yield surface: rotation angle $\alpha = \tan^{-1}\{(1+\sin\phi)/(1-\sin\phi)\}$ from σ_3. Vector magnitude is scaled relative to shear displacement.

result of test UT2 with SS. Test SS exhibits the same mean permeability, over the spatial domain, as UT2. A complete picture of how permeability and temperature evolve from the initially heterogeneous state is provided by Fig. 9. Note the strong hydraulic gradient between injection and withdrawal, causing a more rapid advance of cold water along this gradient. Note also that the permeability field is not smoothed out by the thermal advance but is, in fact, exacerbated by it.

7. Permeability mechanisms and short circuiting

This section discusses methods by which two reservoir conceptualizations, exhibiting the same initial uniform permeability can exhibit largely different behaviors as a result of fracture characteristics. This is an important analysis in EGS reservoirs, where the fracture network must be sufficiently permeable to allow rapid fluid exchange, but sufficiently impermeable to allow high thermal residence time.

Tests UT1, UT2, and UT3 each exhibit a uniform permeability of 8.24×10^{-15} m^2 in the x and y directions. UT1 utilizes a fracture with a surface roughness displaying a standard deviation of 0.513 mm. UT2 and UT3 exhibit a surface standard deviation of 1.538 and 2.563 mm, respectively. In a traditional continuum modeling formulation, these tests would differ in a few ways, but would not exhibit dramatically different circulation characteristics. Dual porosity flow, accommodated in TOUGHREACT, allows for the mean diffusive length and volume between the fracture and matrix domains to differ as a function of fracture spacing. Therefore, thermal and hydraulic transfer between fracture and matrix will differ for different fracture spacings. However, for flow within the fracture domain alone Darcy's law will predict the same flow behavior for each case. Dual porosity poroelasticity, accommodated in the interpolation module, is derived based upon relative volume fractions between the fracture and matrix. This will also partially accommodate differences by more correctly addressing the transfer of pressure between domains. The fracture closure model, however, allows much more significant differences between these two cases to be highlighted.

Because UT1 and UT2 exhibit different spatial roughness scales, their shear dilation behavior will differ, as will the rate of contact area change for a given amount of compression or dilation (and thus differences in specific stiffness). For a given amount of shear, a larger-scale fracture will dilate more severely. A smaller-scale fracture will dilate by a lesser amount, but because a smaller fracture spacing is required to achieve an identical permeability, this dilation will occur over a larger number of fractures; thus amplifying the effect. As permeability scales with the cube of fracture aperture, a small amount of shear in a significantly rough fracture can lead to extremely large permeability changes.

Figs. 10 and 11 examine advancement of the thermal front and changes to withdrawal rate as a function of the different fracture characteristics of UT1 and UT2. The slower thermal advance (Fig. 10) of UT1 represents a more desirable situation for higher fluid residence times, while the higher withdrawal rate (Fig. 11) of UT2 is beneficial for energy recovery in the near term. While UT2 exhibits a quicker thermal advance, it nonetheless takes ~15 years to achieve any thermal breakthrough at the withdrawal well located 500 m away. However, if the often quoted feasibility guideline of 80 kg/s [25] withdrawal rate is achieved, obvious consequences will settle in on this breakthrough time. Furthermore, the thermal stresses that arise in these simulations at near 15 kg/s lead to increases in permeability greater than two orders of magnitude at the injection well and within the advancing
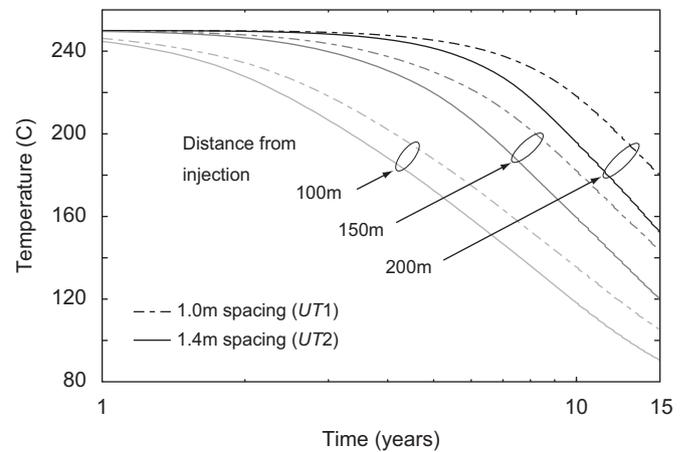

Fig. 10. Transient advance of temperature at three locations within the reservoir between injection and withdrawal. Compares small features of tight spacing (UT1) with moderate features of less frequent spacing (UT2).
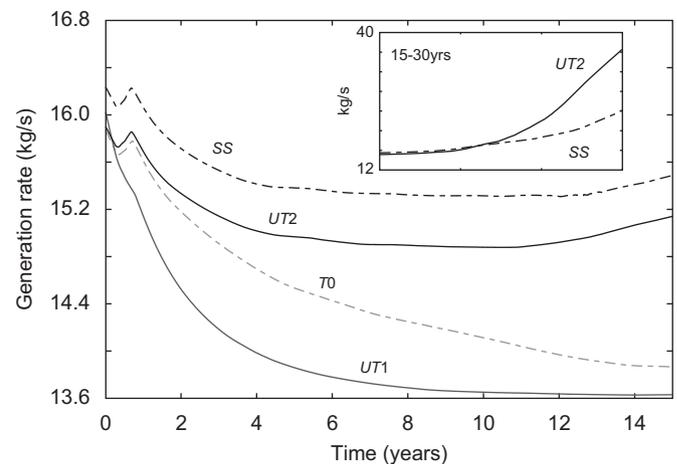

Fig. 11. Evolution in generation rate for all tests. Insert shows longer term analysis for UT2 and SS.

permeability field (Fig. 9). If the fractures are smaller scale, higher spatial frequency (UT1) then this increase is not undesirable. If they are larger scale, lower frequency (UT3), the result may be closer to what is shown in Fig. 12.

The introduction of UT3 in Fig. 12 shows potential short-circuiting behavior. UT3 was ceased after 2.5 years of simulation due to permeability increases of such a magnitude (and at a significant distance from the well, ~150 m at 2.5 years) that the rate of thermal advance and resulting thermal stress decreased the simulation time step to nearly infeasible, without showing signs of slowing. This is a significant increase in permeability enhancement behavior beyond the trend shown by UT1 and UT2, and suggests a possible mechanism for short circuiting; not via fracture propagation, but through the reactivation of large-scale relic fractures.

8. Contributing mechanisms and preferential pathways

Preferential flow pathways visible in Fig. 9 are similar to those observed in [60] due to the action of thermal stress on the fracture system. The methodology and results of both papers make clear the importance not only of bulk permeability, but also of fracture
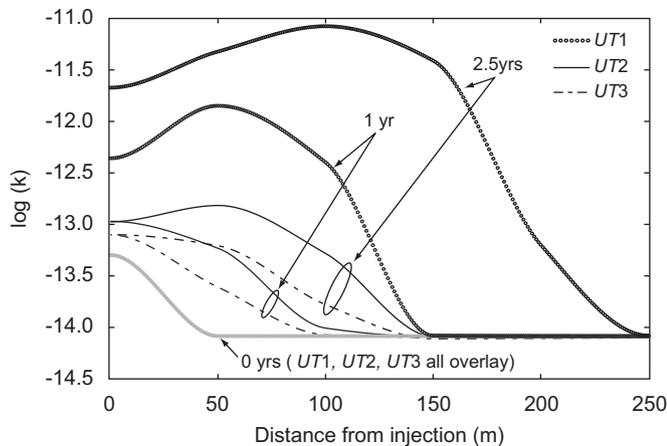
Fig. 12. Permeability evolution with distance from injection at select times. Compares small tight fractures (UT1) against moderate fractures (UT2) and larger scale, loosely spaced fractures (UT3).

Fig. 13. Relation between pressure solution and shear dilation. A single fracture (NV1) is sheared at several increments, and allowed to equilibrate following each event. L is sample length and x is shear distance. Each shear event is 0.07% of sample length. Aperture change due to elastic compression, Δb_E, is shown on lower line.

frequency and scale (even for identical magnitudes of initial bulk permeability) in determining the potential for fluid/thermal short circuiting. Order of magnitude changes in permeability are observable due to thermal stresses. Permeability is an extremely dynamic property in these environments, and THM couplings are clearly a requirement in attempting to model fluid circulation behavior. In addition, the current work and that of [57] illustrate that chemical and/or chemical–mechanical effects can be equally important.

Overall, determining the potential for short circuiting is an extremely complex endeavor. While shear dilation is clearly the dominant permeability change mechanism in these simulations, it is inherently impacted by thermal transfer, which is dependent on hydromechanical and chemical processes that alter fracture permeability. Examining timescales of the onset of these processes, as in [57], may be useful in determining guidelines for how they interact.

8.1. Relationship between fracture shear and pressure solution

The action of pressure solution also deserves some discussion. Following hydraulic fracturing of the injection and withdrawal wells (during which significant fracture shearing occurs) PS is reactivated and compacts the withdrawal region by an additional ~20 µm. This is not visible in the figures because equilibration was conducted prior to beginning reservoir simulation, but indicates that the reactivation of PS along sheared relic fractures may have consequences for permeability. This behavior is illustrated in further detail in Fig. 13.

A simulation is conducted in a single fracture (NV1), as in Fig. 5. The fracture is sheared (numerically) a small amount to generate elevated permeability, as in hydraulic fracturing. This process alters significantly the characteristics of the contacting fracture, potentially reactivating the pressure solution process. The fracture is then allowed to re-equilibrate to pressure solution equilibrium. We perform this process in several cycles and the results demonstrate that pressure solution may be a crucial factor in permeability evolution for systems pushed into disequilibrium.

This evaluation is performed with a fully implicit simulation [41] of pressure solution, rather than using the simplification of Eq. (5), so that dissolution and diffusion at fracture contacts are considered. Most of the pressure solution compaction occurs quite rapidly within the sample, but time to the complete equilibration is on the order of years. This is due to a transition
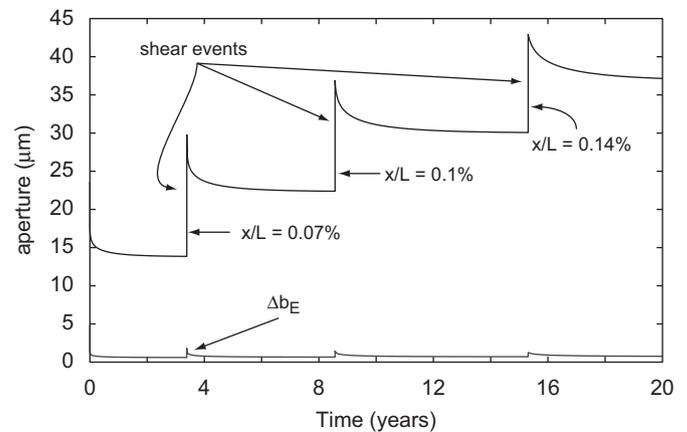
into a much slower regime dominated by chemical diffusion as the fracture compacts and contact area increases, and indicates that a more complete model than the equilibrium form presented above may be needed to examine this long-term behavior.

9. Discussion

A model for the combined action of elastic deformation, stress-enhanced dissolution, and shear dilation has been developed. This model was successfully implemented within a reservoir scale THMC simulator to follow the evolution of an EGS reservoir. Simulations conducted in pseudo-3D do not show a strong impact of truly anisotropic permeability evolution; a conclusion that may differ in a fully 3D system. Heterogeneity in permeability, generated from a normal distribution of fracture spacing, does have consequences for thermal breakthrough times at the withdrawal well, as well as for withdrawal rates. For the given conditions, spatial variability over ~1 order of magnitude leads to a reduction of ~10% in withdrawal rates compared to a spatially uniform system, although this result will likely differ depending on characteristics of the heterogeneity.

The new permeability mechanism is capable of distinguishing differences between (1) small scale, frequent fractures and (2) large scale, more widely spaced fractures. A given magnitude of permeability due to widely spaced, highly conductive fractures exhibits strongly different behavior than the same bulk permeability magnitude, derived from tightly spaced, lower conductivity fractures.

Fracture shear and dilation is the most significant contributor to permeability change at the conditions examined here. Pressure solution contributes to system behavior following a large shift from equilibrium, such as after a hydraulic stimulation, but has less impact on the evolution of the reservoir beyond this limited zone. Elastic deformation and chemical behaviors have a similar impact in the long term. Previous results showing the eventual shutdown of injection due to mineral precipitation at long timescales [57] may be counteracted by shear dilation, but this is a conclusion that is highly dependent on reinjected aqueous concentrations: a parameter that was not varied in the above analysis. Laboratory studies are needed beyond those currently reported to resolve questions of the importance of pressure solution in rough fractures and at geothermal conditions to further constrain their influence.

Acknowledgements

References

[1] Goodman RE. Methods of geological engineering in discontinuous rocks. New York: West Publishing; 1976.

[2] Walsh JB. Effect of cracks on uniaxial elastic compression of rocks. J Geophys Res 1965:399–411.

[3] Taron J, Elsworth D, Min KB. Numerical simulation of thermal–hydrologic–mechanical–chemical processes in deformable, fractured porous media. Int J Rock Mech Min Sci 2009;46(5):842–54.

[4] Elsworth D. Thermal permeability enhancement of blocky rocks: plane and radial flow. Int J Rock Mech Min Sci 1989;26:329–39.

[5] Elsworth D, Xiang J. A reduced degree of freedom model for thermal permeability enhancement in blocky rocks. Geothermics 1989;18:691–709.

[6] Brown SR, Scholz CH. Closure of rock joints. J Geophys Res 1986;91(B5):4939–48.

[7] Barton N, Bandis S, Bakhtar K. Strength deformation, and conductivity coupling of rock joints. Int J Rock Mech Min Sci 1985;22(3):121–40.

[8] Elsworth D, Goodman RE. Characterization of rock fissure hydraulic conductivity using idealized wall roughness profiles. Int J Rock Mech Min Sci 1986;23(3):233–43.

[9] Gangi AF. Variation of whole and fractured porous rock permeability with confining pressure. Int J Rock Mech Min Sci 1978;15(5):249–57.

[10] Olsson R, Barton N. An improved model for hydromechanical coupling during shearing of rock joints. Int J Rock Mech Min Sci 2001;38(3):317–29.

[11] Yeo IW, De Freitas MH, Zimmerman RW. Effect of shear displacement on the aperture and permeability of a rock fracture. Int J Rock Mech Min Sci 1998;35(8):1051–70.

[12] Zimmerman RW, Bodvarsson GS. Hydraulic conductivity of rock fractures. Trans Porous Media 1996;23(1):1–30.

[13] Renshaw CE. On the relationship between mechanical and hydraulic apertures in rough-walled fractures. J Geophys Res 1995;100(B12):24629–36.

[14] Piggott AR, Elsworth D. Laboratory assessment of the equivalent apertures of a rock fracture. Geophys Res Lett 1993;20(13):1387–90.

[15] Detwiler RL. Experimental observations of deformation caused by mineral dissolution in variable-aperture fractures. J Geophys Res 2008;113(B8).

[16] Peters CA. Accessibilities of reactive minerals in consolidated sedimentary rock: an imaging study of three sandstones. Chem Geol 2009;265(1–2):198–208.

[17] Paterson MS. Nonhydrostatic thermodynamics and its geologic applications. Rev Geophys 1973;11(2):355–89.

[18] Tada R, Siever R. Pressure solution during diagenesis. Ann Rev Earth Planet Sci 1989;17:89–118.

[19] Atkinson BK, Meredith PG. The theory of subcritical crack growth with applications to minerals and rocks. In: Atkinson BK, editor. Fracture mechanics of rock. San Diego: Academic Press; 1987.

[20] Niemeijer A, Spiers CJ, Bos B. Compaction creep of quartz sand at 400–600 degrees C: experimental evidence for dissolution-controlled pressure solution. Earth Planet Sci Lett 2002;195(3–4):261–75.

[21] Beeler NM, Hickman SH. Stress-induced time-dependent fracture closure at hydrothermal conditions. J Geophys Res 2004;109(B2).

[22] Polak A, Elsworth D, Yasuhara H, et al. Permeability reduction of a natural fracture under net dissolution by hydrothermal fluids. Geophys Res Lett 2003;30:20.

[23] Schutjens PMTM. Experimental compaction of quartz sand at low effective stress and temperature conditions. J Geol Soc 1991;148:527–39.

[24] Chester FM, Chester JS, Kronenberg AK, et al. Subcritical creep compaction of quartz sand at diagenetic conditions: effects of water and grain size. J Geophys Res 2007;112(B6).

[25] Tester J, Anderson BJ, Batchelor AS, et al. The future of geothermal energy: impact of enhanced geothermal systems (EGS) on the United States in the 21st century. Cambridge, MA: Massachusetts Institute of Technology; 2006.

[26] Rutqvist J, Wu YS, Tsang CF, et al. A modeling approach for analysis of coupled multiphase fluid flow, heat transfer, and deformation in fractured porous rock. Int J Rock Mech Min Sci 2002;39(4):429–42.

[27] Min KB, Rutqvist J, Elsworth D. Chemically and mechanically mediated influences on the transport and mechanical characteristics of rock fractures. Int J Rock Mech Min Sci 2009;46(1):80–9.

[28] Jaeger JC, Cook NGW, Zimmerman RW. Fundamentals of rock mechanics. 4th ed.. Malden, MA: Blackwell; 2007.

[29] Lee SD, Harrison JP. Empirical parameters for non-linear fracture stiffness from numerical experiments of fracture closure. Int J Rock Mech Min Sci 2001;38(5):721–7.

[30] Pyrak-Nolte LJ, Morris JP. Single fractures under normal stress: the relation between fracture specific stiffness and fluid flow. Int J Rock Mech Min Sci 2000;37(1–2):245–62.

[31] McDermott C, Kolditz O. Geomechanical model for fracture deformation under hydraulic, mechanical and thermal loads. Hydrogeol J 2006;14(4):485–98.

[32] Beeler NM, Hickman SH. A note on contact stress and closure in models of rock joints and faults. Geophys Res Lett 2001;28(4):607–10.

[33] Hopkins DL. The effect of surface roughness on joint stiffness, aperture, and acoustic wave propagation. PhD Thesis, Berkeley: University of California; 1991.

[34] Cook NGW. Natural joints in rock: mechanical, hydraulic and seismic behavior and properties under normal stress. Int J Rock Mech Min Sci Geomech Abstr 1992;29(3):198–223.

[35] Brown SR, Scholz CH. Closure of random elastic surfaces in contact. J Geophys Res 1985;90(NB7):5531–45.

[36] Piggott AR, Elsworth D. Analytical models for flow through obstructed domains. J Geophys Res 1992;97(B2):2085–93.

[37] Swan G. Determination of stiffness and other joint properties from roughness measurements. Rock Mech Rock Eng 1983;16(1):19–38.

[38] Dewers T, Ortoleva P. Force of crystallization during the growth of siliceous concretions. Geology 1990;18(3):204–7.

[39] Revil A. Pervasive pressure-solution transfer: a poro-visco-plastic model. Geophys Res Lett 1999;26(2):255–8.

[40] Stephenson LP, Plumley WJ, Palciauskas VV. A model for sandstone compaction by grain interpenetration. J Sedim Petrol 1992;62(1):11–22.

[41] Taron J, Elsworth D. Constraints on compaction rate and equilibrium in the pressure solution creep of quartz aggregates and fractures: controls of aqueous concentration. J Geophys Res 2010:115.

[42] Gundersen E, Renard F, Dysthe DK, et al. Coupling between pressure solution creep and diffusive mass transport in porous rocks. J Geophys Res 2002;107(B11).

[43] Rutter EH. Kinetics of rock deformation by pressure solution. Philos Trans R Soc London Ser A 1976;283(1312):203–19.

[44] Yasuhara H, Elsworth D, Polak A. A mechanistic model for compaction of granular aggregates moderated by pressure solution. J Geophys Res 2003;108(B11).

[45] Revil A. Pervasive pressure solution transfer in a quartz sand. J Geophys Res 2001;106(B5):8665–86.

[46] Poulos HG, Davis EH. Elastic solutions for soil and rock mechanics. New York: Wiley; 1974.

[47] Borodich FM. Fractals and fractal scaling in fracture mechanics. Int J Fracture 1999;95(1–4):239–59.

[48] Borri-Brunetto M, Carpinteri A, Chiaia B. Scaling phenomena due to fractal contact in concrete and rock fractures. Int J Fracture 1999;95(1–4):221–38.

[49] Zhou HW, Xie H. Direct estimation of the fractal dimensions of a fracture surface of rock. Surf Rev Lett 2003;10(5):751–62.

[50] Schmittbuhl J, Gentier S, Roux S. Field-measurements of the roughness of fault surfaces. Geophys Res Lett 1993;20(8):639–41.

[51] Xu TF, Sonnenthal E, Spycher N, et al. TOUGHREACT—a simulation program for non-isothermal multiphase reactive geochemical transport in variably saturated geologic media: applications to geothermal injectivity and CO_2 geological sequestration. Comput Geosci 2006;32(2):145–65.

[52] Itasca. FLAC3D manual: fast lagrangian analysis of continua in 3 dimensions—version 2.0. Minneapolis: Itasca Consulting Group; 1997.

[53] Berryman JG, Wang HF. The elastic coefficients of double-porosity models for fluid transport in jointed rock. J Geophys Res 1995;100(B12):24611–27.

[54] Elsworth D, Bai M. Flow-deformation response of dual-porosity media. J Geotech Eng 1992;118(1):107–24.

[55] Sheridan JM, Hickman SH. In situ stress, fracture, and fluid flow analysis in wel 38C-9: an enhanced geothermal system in the Coso geothermal field. In: Proceedings of the 29th workshop on geothermal reservoir engineering, Stanford University, 2004.

[56] Kovac KM, Xu TF, Pruess K, et al. Reactive chemical flow modeling applied to injection in the Coso EGS experiment. In: Proceedings of the 31st workshop geothermal reservoir engineering, Stanford University, 2006.

[57] Taron J, Elsworth D. Thermal-hydrologic-mechanical-chemical processes in the evolution of engineered geothermal reservoirs. Int J Rock Mech Min Sci 2009;46(5):855–64.

[58] Watanabe N, Wang WQ, McDermott CI, et al. Uncertainty analysis of thermo-hydro-mechanical coupled processes in heterogeneous porous media. Comput Mech 2010;45(4):263–80.

[59] Bear J. Modeling flow and contaminant transport in fractured rocks. In: Bear J, de Marsily G, Tsang CF, editors. Flow and contaminant transport in fractured rock. San Diego: Academic Press; 1993.

[60] McDermott CI, Randriamanjatosoa ARL, Tenzer H, et al. Simulation of heat extraction from crystalline rocks: the influence of coupled processes on differential reservoir cooling. Geothermics 2006;35(3):321–44.